Impact of momentum mismatch on 2D van der Waals tunnel field-effect transistors

Impact of momentum mismatch on 2D van der Waals tunnel field-effect transistors

Jiang Cao[1,2], Demetrio Logoteta[3], Marco G. Pala[4] and Alessandro Cresti[1]

[1] Univ. Grenoble Alpes, CNRS, Grenoble INP, IMEP-LaHC, F-38000 Grenoble, France

[2] Tyndall National Institute, Dyke Parade, Cork, Ireland

[3] IM2NP UMR 7334, CNRS, Aix Marseille Université, Marseille, France

[4] Centre de Nanosciences et de Nanotechnologies, CNRS, Univ. Paris-Sud,Université Paris-Saclay, 91405 Orsay, France

Abstract. We numerically investigate electron quantum transport in 2D van der Waals tunnel field-effect-transistors in the presence of lateral momentum mismatch induced by lattice mismatch or rotational misalignment between the two-dimensional layers. We show that a small momentum mismatch induces a threshold voltage shift without altering the subthreshold swing. On the contrary, a large momentum mismatch produces significant potential variations and ON-current reduction. Short-range scattering, such as that due to phonons or system edges, enables momentum variations, thus enhancing interlayer tunneling. The coupling of electrons with acoustic phonons is shown to increase the ON current without affecting the subthreshold swing. In the case of optical phonons, the ON-current increase is accompanied by a subthreshold swing degradation due to the inelastic nature of the scattering.

Keywords: tunnel field-effect-transistor, non-equilibrium Green's function, 2D transition metal dichalcogenides, van der Waals heterostructures.

1. Introduction

Low-power logic devices [1] such as tunnel field-effect-transistors (TFETs) can enable a very aggressive scaling of the supply voltage (V_{DD}) by reducing the subthreshold swing (SS) below the thermionic limit of 60 mV/dec at room temperature. Despite the promising experimental results reported for Si and III-V TFETs [2, 3, 4, 5], these devices are very demanding in terms of gate control and electrostatic integrity [6, 7], and their OFF-state performance can be seriously degraded by inelastic trap-assisted tunneling induced by interface or bulk defects [8, 9]. Van der Waals (vdW) heterostructures of 2D materials show an excellent potential for vertical TFET applications [10, 11, 12, 13, 14, 15, 16], since they may overcome some of the above issues [17, 18] thanks to their atomic thinness and the absence of dangling bonds, and offer, at same time, a very large variety of band alignments [19]. After the experimental demonstration of vdW Esaki diodes [20, 21], the first sub-thermionic device was realized by a heterojunction of MoS_2 and bulk Ge [22]. The SS of vertical TFETs obtained from vdW heterojunctions of 2D materials typically situates between 150 mV/dec and 100 mV/dec [23]. Very recently, a TFET based on a multilayer $SnSe_2/WSe_2$ heterojunction has been demonstrated to achieve an average SS around 80 mV/dec over two decades of current, with a subthermionic minimum SS of 37 mV/dec [24]. Moreover, an average SS of 57 mV/dec over two decades of current has been observed in a TFET based on the heterojunction between MoS_2 and black phosphorus [25]. While encouraging, these results call for improved fabrication processes and a careful device design.

Lattice mismatch and rotational misalignment of the layers might represent common critical sources of disorder, which can severely affect the interlayer coupling, as indicated in the case of bilayer graphene [26], and are hard to control in the fabrication process, especially in stacks obtained by dry transfer methods [27, 28]. In vdW structures of semiconducting 2D materials, misorientation has been shown to modify interlayer coupling and distance [29, 30], as well as in-plane [31] and interlayer transport [32], and even the excitonic properties [33]. The effects of rotational misalignment on vdW-TFETs have previously been investigated by semi-analytical approaches [10]. A recent *ab initio* full-quantum study has shown that misalignment in a ballistic lateral TFET based on an MoS_2-ZrS_2 heterojunction [34] can severely affect the device performance. This is ascribed to the overlap variation between the orbitals of the two layers and to the strong anisotropy in the ZrS_2 band structure, which makes the conduction depend on the transport direction. Here, we investigate the effects of misalignment in transition metal dichalcogenide (TMD) vertical vdW-TFETs based on a different architecture, which have been shown to be promising in previous studies [10, 11, 12, 13]. In most monolayer TMDs, the valleys are located at the hexagonal Brillouin zone (BZ) corners (K-points) [19]. Lattice mismatch and rotational misalignment entail a displacement of the valleys and thus the transition to an indirect band gap system. As observed experimentally and theoretically for graphene bilayer

[35, 36, 37] and predicted for vdW graphene heterojunctions [38], such a lateral momentum mismatch strongly affects the interlayer tunneling, which can be effectively assisted by phonons [39, 40, 41, 42].

In this paper, we study the impact of momentum mismatch on the transport properties of vdW heterojunction TFETs by means of 3D numerical simulations based on the non-equilibrium Green's functions (NEGF) method. Our 3D self-consistent quantum transport simulations take into account the electron-phonon scattering, which we demonstrate to play a major role in this context.

2. Device model and simulation approach

We simulate a vdW-TFET combining an intrinsic WTe_2 bottom layer acting as source and an MoS_2 top layer acting as drain [10, 13], see figure 1(a). This particular choice of TMD materials, which shows a suitable staggered band alignment, is paradigmatic and it is used to provide a general trend and a physical insight into the impact of momentum mismatch on the performance of generic vdW-TFETs. In order to ensure Ohmic contacts, the drain layer is chemically n-doped close to the right drain contact with density N_D and a bottom-gate (at potential V_{BG}) covers the entire bottom layer to electrostatically dope the source layer. The electrostatics in the central overlap region

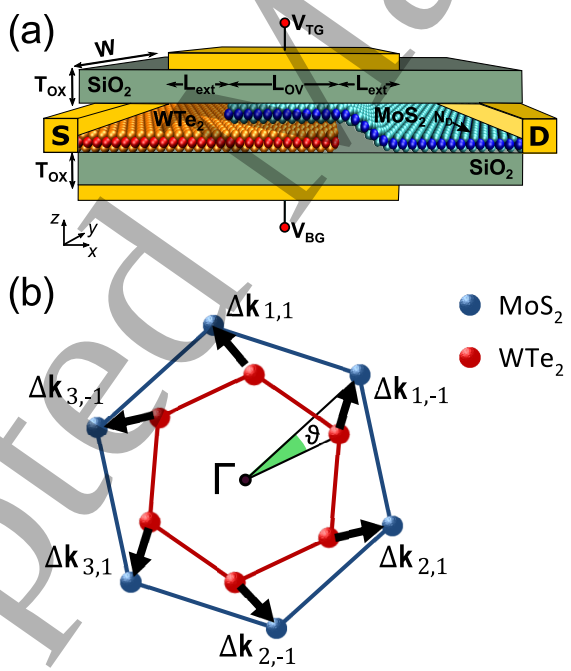

Figure 1. (a) Sketch and main parameters of the vdW-TFET structure. The metallic source (S) and drain (D) contacts are not included in the simulation and replaced by the periodic prolongation of the 2D layers. (b) The Brillouin zones (red and blue hexagons) of the two layers with lattice mismatch and twist angle θ. Note that the size difference between the two BZs has been exaggerated compared to the lattice mismatch between MoS_2 and WTe_2.

(with length L_{OV}) is controlled by a top-gate (at potential V_{TG}) that exceeds the overlap region on each side by the extension length L_{ext}.

When the top and bottom monolayers are stacked together in a heterojunction, the lattice mismatch and the interlayer rotation with angle θ entail the hexagonal BZs of the two layers have different size and are rotated by θ around the Γ-point, see figure 1(b). As a results, the conduction band (CB) extrema are shifted from the corresponding valence band (VB) extrema, see the arrows in figure 1(b), thus resulting in a lateral momentum mismatch between the two layers with a shift $\boldsymbol{\Delta k}_{n,i}$ for the valleys at $\boldsymbol{K}_{n,i}$, where $i = \pm 1$ indexes two nonequivalent K-valleys, and $n = 1,\ 2,\ 3$ indexes three equivalent pairs of K-points in the BZ. Due to the staggered band alignment between the two layers, only the VB of bottom layer and the CB of top layer participate in charge transport. Note that also the top of the VB at Γ may fall within the energy window of electron transport. However, the momentum mismatch between the Γ-valley and the K-valleys is large independently of the rotation angle. Therefore, as illustrated in the rest of the paper, we expect that the tunneling from the valence Γ-valley to the conduction K-valleys is weaker than the tunneling within K-valleys, and we disregard it in our model. Close to the conduction and valence band extrema located at the K-points, the CB and VB have isotropic parabolic energy dispersion. A two-band effective-mass model can thus provide a reasonable description of the band structure in the energy range for electron transport around the gap. The model Hamiltonian for each couple of CB and VB valleys has the form

$$\mathbf{H}_{n,i} = \begin{pmatrix} -\frac{|\boldsymbol{p}|^2}{2m_{\mathrm{v}}} + eU_{\mathrm{B}}(\boldsymbol{r}) - \Delta & t_\perp \\ t_\perp & \frac{|\boldsymbol{p}-\hbar\boldsymbol{\Delta k}_{n,i}|^2}{2m_{\mathrm{c}}} + eU_{\mathrm{T}}(\boldsymbol{r}) \end{pmatrix}, \tag{1}$$

where the diagonal terms describe the isolated 2D layers, m_{v} (m_{c}) is the effective mass of the valence (conduction) band, $\boldsymbol{r} = (x, y)$ is the in-plane position vector, $\boldsymbol{p} = -i\hbar(\partial_x, \partial_y)$ is the in-plane momentum operator, Δ gives the energy separation between VB and CB (interlayer band gap), U_{T} and U_{B} expresses the electrostatic potentials on the top and bottom layers, which are obtained by self-consistently coupling the quantum transport equation with the Poisson equation, and $t_\perp$ is the interlayer coupling energy. As shown by Liu *et al* [43], in homojunctions the repulsive steric effects between the two 2D layers change the interlayer distance and coupling for different stacking configurations. However, due to lattice mismatch present in heterojunctions, the atoms of the top layer sit nearly randomly relative to the atoms of the bottom layer. This is analogous to what happens for homojunction with large rotational misalignment [43, 30, 44]. As a consequence, while the interlayer distance and coupling can spatially vary due to the variation of local layer stacking patterns [45, 46], their average values are not very sensitive to the global stacking configuration. Therefore, since the considered TFETs are based on heterojunctions, we approximate $t_\perp$ as independent of the stacking configuration. Moreover, since the Fourier transform of the interatomic coupling decays at large wave-vectors [47], we just take into account the interband coupling within the couples of valleys in the first Brillouin zone. More sophisticated models, taking into

m_c/m_e	m_v/m_e	$t_\perp$	Δ	D_{ac}	D_{op}	$\hbar\omega_{op}$
0.391	0.543	6 meV	134 meV	3 eV	2.6×10^8 eV/cm	50 meV

Table 1. Parameters of the model Hamiltonian, see [13, 48].

account the dependence of the interlayer coupling on both the wave vector and the stacking details, can be found, for example, in [45, 47].

The electron-phonon coupling is modeled by means of an intravalley acoustic (D_{ac}) and optical (D_{op}) deformation potentials and by assuming a single optical phonon energy $\hbar\omega_{op}$ corresponding to the energy of the most coupled optical phonon mode (A_{1g}) [48]. This simple model allows us to qualitatively describe the effect of the electron-phonon coupling in this type of transistors, while avoiding the heavy computational burden required to take into account the strongly material- and geometry-dependent effect of interlayer and substrate coupling on the phonon dispersion and on the deformation potential. In order to give an idea of how different electron-phonon coupling strengths would affect the vdW-TFET properties, at the end of next section, we consider several values for the phonon deformation potentials. Table 1 reports all the parameters used in the model and their values, extracted from DFT calculations, which refer to the paradigmatic couple of materials (WTe_2 and MoS_2) we consider.

To solve the transport problem, we make use of the Keldysh-Green's function formalism within the coupled-mode space approach [49, 50] applied to the discretized form of the real-space Hamiltonian. We used a finite difference discretization with a step size of 0.2 nm. The retarded ($\mathbf{G^R}$) and lesser ($\mathbf{G^<}$) Green's functions are obtained as

$$(E\mathbf{I}-\mathbf{H}-\mathbf{\Sigma^R})\mathbf{G^R}=\mathbf{I} \quad \text{and} \quad \mathbf{G^<}=\mathbf{G^R}\mathbf{\Sigma^<}\mathbf{G^{R\dagger}}\ , \tag{2}$$

where E is the electron energy, $\mathbf{I}$ is the identity matrix, the self-energies $\mathbf{\Sigma^R}$ and $\mathbf{\Sigma^<}$ account for the coupling with source and drain contacts and for the electron-phonon interaction. The phonon self-energies are computed within the self-consistent Born approximation [51]. The lesser-than self-energy for acoustic phonons reads

$$\mathbf{\Sigma^<_{ac}}_{i,i}(E)=\frac{D_{ac}^2 k_B T}{\rho v_s^2}\mathbf{G}^<_{i,i}(E)\ , \tag{3}$$

where i indexes the site, ρ is the mass density, v_s is the sound velocity, k_B is the Boltzmann constant and T is the temperature, which we set to 300 K. The non-polar optical phonon lesser-than self-energy reads

$$\mathbf{\Sigma^<_{op}}_{i,i}(E)=\frac{\hbar D_{op}^2}{2\rho\omega_{op}}\left\{\mathbf{G}^<_{i,i}(E+\hbar\omega_{op})[N(\omega_{op},T)+1]+\mathbf{G}^<_{i,i}(E-\hbar\omega_{op})N(\omega_{op},T)\right\}\ , \tag{4}$$

where $N(\omega_{op},T)$ is the equilibrium phonon distribution according to the Bose statistics. The charge density obtained from $\mathbf{G^<}$ is passed as input to the 3D Poisson equation solver that computes the electrostatic potential on a finite element mesh. The procedure is repeated up to convergence and the current is finally extracted. We consider a channel width $W = 20$ nm, an overlap region with length L_{OV}=20 nm, an extension

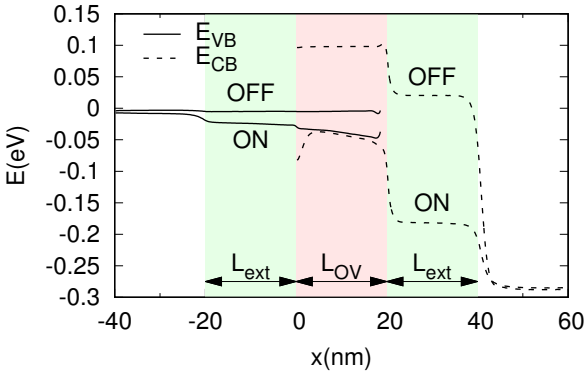

Figure 2. Conduction (E_{CB}) and valence (E_{VB}) band edges along the transport direction x, see figure 1, for V_{TG}= 0 V (OFF state) and 0.3 V (ON state) for Δk=0. The source Fermi level is at 0 eV and the drain Fermi level is at −0.3 eV. The shadowed areas indicate the overlap and extension regions.

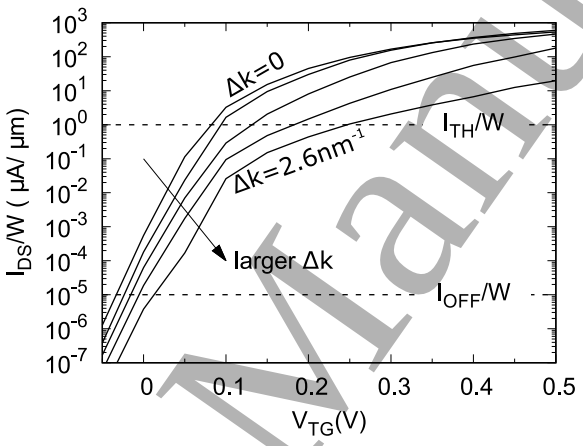

Figure 3. Current *per* unit width I_{DS}/W as a function of the top gate potential for momentum mismatch $0 \leq \Delta k \leq 2.6$ nm^{-1}.

length for the top gate L_{ext}=20 nm, oxide thickness T_{OX}=1 nm and relative permittivity κ=3.9, a doping for the drain contact (outside the overlap and the extension regions) $N_{\mathrm{D}} = 4 \times 10^{12}$ cm^{-2}, both gates in Al, a bottom gate potential V_{BG}=-0.5 V (this value ensures the source layer to be degenerate and shifts the OFF-state V_{TG} of the device close to 0), and a source-drain bias V_{DS}=V_{DD}=0.3 V.

3. Results and discussion

The device working principle is illustrated in figure 2, which shows the valence and conduction band edge profile along the transport direction in the ON and the OFF states. In the OFF state, the CB edge of the top layer (E_{CB}) is higher than the VB edge of the bottom layer (E_{VB}). Therefore, after tunneling into the top layer, the electrons injected from the source fall into the band gap of top (MoS_2) layer and their transmission through the extension region is exponentially suppressed with L_{ext} [13]. While increasing the top-gate voltage, E_{CB} drops faster than E_{VB} due to the larger

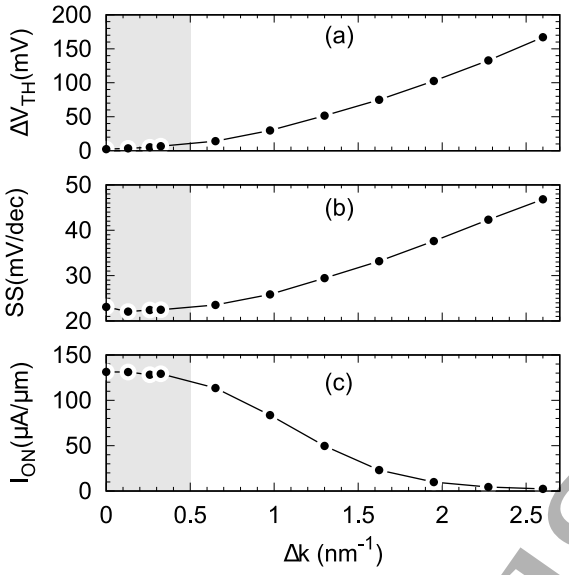

Figure 4. Threshold voltage variation (a), average subthreshold swing (b) and ON current *per* unit width (c) as a function of the momentum shift Δk. For small momentum mismatch $\Delta k \lesssim 0.5$ nm^{-1} (shadowed area), the system preserves the characteristics of the perfectly aligned layers.

capacitance coupling between the top layer and the top-gate. When E_{CB} and E_{VB} cross, an energy window allowing electrons to tunnel opens and I_{DS} rapidly increases. The crossing of E_{CB} and E_{VB} determines the threshold voltage, which thus depends on the specific couple of TMDs chosen and on the gate metal, through the interlayer band gap Δ and the metal work function, respectively.

In what follows, we consider the momentum mismatch $\boldsymbol{\Delta k}_{n,i}$ induced by lattice mismatch and twist angle. For the sake of simplicity, we quantify the momentum mismatch as if it were generated by a twist angle θ in the absence of lattice mismatch (the lattice parameter of WTe_2 is assumed equal to that of MoS_2). The investigated range $0 \leq \Delta k = |\boldsymbol{\Delta k}_{n,i}| \leq 2.6$ nm^{-1} would correspond (almost linearly) to angles in the range $0 \leq \theta \leq 20°$. We notice that, independently of the angle, Δk cannot go down to zero for the specific couple of materials considered, due to the lattice mismatch. The range of Δk values close to zero is nevertheless investigated in this paper, since it can elucidate the impact of small Δk in other couples of TMDs with closer lattice parameters.

Figure 3 illustrates the transfer characteristic I_{DS}-V_{TG} of the device for different values of the momentum mismatch. At given top gate voltage V_{TG}, the mismatch entails a significant current decrease. This is due to the interlayer tunneling reduction caused by the shift between the valleys, and the consequent larger momentum change required for the electrons to pass from WTe_2 to MoS_2. Remarkably, the impact on the subthreshold swing is quite modest for $V_{\mathrm{TG}} \lesssim 0.1$ V, i.e. deep in the OFF state, before the band crossing. As detailed in [13], in ideal conditions the steep slope of vdW-TFET is determined by intralayer tunneling through the extension region, which

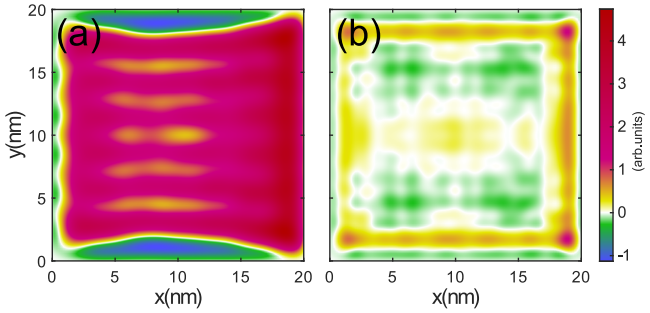

Figure 5. Spatial distributions of the interlayer tunneling current density in the overlap region for V_{TG}= 0.4 V and (a) Δk=1.3 nm^{-1}, (b) Δk=2.6 nm^{-1}.

is not affected by Δk. This latter simply reduces the interlayer tunneling probability, thus resulting in a vertical shift of the subthreshold characteristics and in the variation of the threshold voltage V_{TH}, see figure 4(a), calculated at the threshold current *per* unit width $I_{\mathrm{TH}}/W = 1$ μA/μm. The threshold voltage shift depends in an almost quadratic way on Δk and can be fit as $\Delta V_{\mathrm{TH}} \approx \hbar^2(1/m_{\mathrm{c}} + 1/m_{\mathrm{v}})\Delta k^2(1 - 0.1\Delta k)$ mV (with Δk in nm^{-1}), which reflects the quadratic energy dispersion of valence and conduction bands. As seen in figure 4(b), for $\Delta k \gtrsim 0.5$ nm^{-1} the current reduction eventually degrades the device average SS, which is evaluated in the fixed window between the OFF current *per* unit width $I_{\mathrm{OFF}}/W = 10^{-5}$ μA/μm and the threshold current *per* unit width I_{TH}/W. In the ON state, the vdW-TFET transport properties depend considerably on Δk. For relatively small Δk, the valley shift is moderate and electrons can still easily tunnel from the valence to the conduction band thanks to the electron-phonon scattering. Therefore, apart from the shift of the characteristic curves, we observe similar current and transconductance for the device with or without misalignment, and the ON current (I_{ON}), calculated at V_{TG}=V_{OFF}+V_{DD}, where V_{OFF} is the top-gate voltage corresponding to I_{OFF}, is almost constant, see figure 4(c). However, I_{ON} starts to exponentially decay when increasing Δk above 1.3 nm^{-1}, with a degradation higher than 85% for $\Delta k \gtrsim 2$ nm^{-1}. To better analyze these two regimes, figure 5 shows the interlayer tunneling current density in the overlap region for the vdW-TFET in the ON state with Δk =1.3 nm^{-1} and Δk =2.6 nm^{-1}. For relatively small Δk, the tunneling occurs quite uniformly inside the overlap region, see figure 5(a). On the contrary, at larger Δk, the tunneling is concentrated at the edges of the overlap region, see figure 5(b), while it is very weak in the central area due to the fact that phonons alone are not able to scatter the electrons over the large Δk. Conversely, the sharp edges of the overlap region are source of short-range scattering, and thus allow the electrons to change their momentum and tunnel between the bands. Such a restricted spatial tunneling distribution further decreases the current and results in the observed poor device performance.

As mentioned above, phonons are an important source of scattering, which can assist interlayer tunneling. To better understand their role, we consider the most unfavorable configuration (Δk=2.6 nm^{-1}) investigated for the vdW-TFET and artificially increase the deformation potential for acoustic and optical phonons. Figure 6

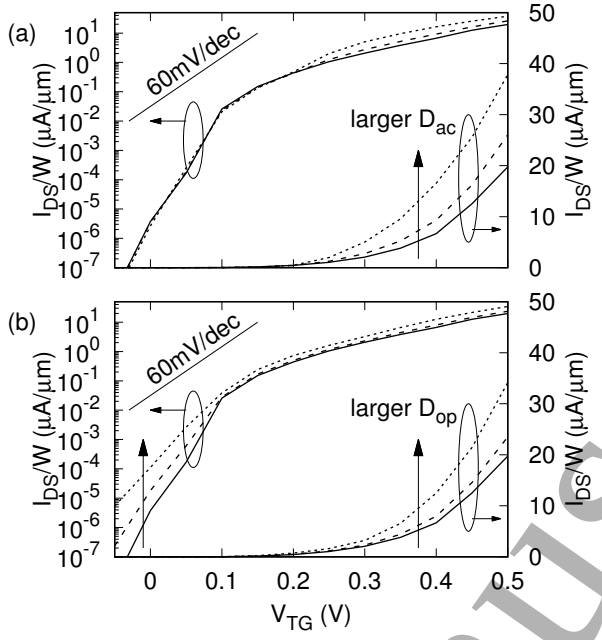

Figure 6. Current *per* unit width as a function of the top gate potential for $\Delta k = 2.6$ nm^{-1} and different values of (a) acoustic deformation potential $D_{\rm ac}$= 3, 6 and 12 eV and (b) optical deformation potential $D_{\rm op}$= 2.6, 5.2 and 10.4×10^8 eV/cm.

shows that increasing the phonon scattering strength results in a substantial ON-current increase. Two possible mechanisms can enhance the electron tunneling, namely the change of momentum of electrons and their promotion to higher energy levels due to the inelastic scattering with optical phonons. As expected, the acoustic phonons do not affect the current in the subthreshold region, see figure 6(a), since, in the elastic approximation of equation (3), they are not able to transfer energy to electrons. On the contrary, inelastic scattering with optical phonons, see equation (4), degrades the SS as shown in figure 6(b), by promoting bottom-layer electrons to higher energies and thus making OFF-state tunneling easier [13].

4. Conclusion

In conclusion, by performing 3D self-consistent full-quantum NEGF simulations of a vdW-TFET, we demonstrated that (i) a small momentum mismatch is expected to slightly affect the device performance through a small threshold voltage variation; (ii) a large momentum mismatch is expected to severely impact the device performance, and to result in a significant reduction of the ON current, a degradation of the subthreshold swing and a rather large threshold voltage variation. The momentum variation necessary to assist interlayer tunneling can be provided by short-range disorder, which is introduced, in our model, by the electron-phonon coupling and by the sharp structure edges. The presence of further short-range scattering sources, as impurities or lattice dislocations, would enhance the interlayer tunneling, but also unavoidably reduce

the intralayer mobility and hence the ON current. Despite the simplicity of the model, our results are quite general and shed light on the main physical mechanisms at play in vdW-TFETs with misoriented layers.

Acknowledgments

This work was partially funded by the French ANR via the project n. ANR-13-NANO-0009-01 "NOODLES".

References

[1] Cristoloveanu S, Wan J and Zaslavsky A 2016 *IEEE Journal of the Electron Devices Society* **4** 215–226 ISSN 2168-6734

[2] Dewey G, Chu-Kung B, Boardman J, Fastenau J M, Kavalieros J, Kotlyar R, Liu W K, Lubyshev D, Metz M, Mukherjee N, Oakey P, Pillarisetty R, Radosavljevic M, Then H W and Chau R 2011 Fabrication, characterization, and physics of III-v heterojunction tunneling field effect transistors (h-TFET) for steep sub-threshold swing *2011 International Electron Devices Meeting* (Institute of Electrical and Electronics Engineers (IEEE)) pp 3361–3364 ISSN 0163-1918

[3] Zhou G, Li R, Vasen T, Qi M, Chae S, Lu Y, Zhang Q, Zhu H, Kuo J M, Kosel T, Wistey M, Fay P, Seabaugh A and Xing H 2012 Novel gate-recessed vertical inas/gasb tfets with record high i_{on} of 180 μA/μm at v_{ds}=0.5 V *2012 International Electron Devices Meeting* pp 3261–3264 ISSN 0163-1918

[4] Knoll L, Zhao Q T, Nichau A, Trellenkamp S, Richter S, Schäfer A, Esseni D, Selmi L, Bourdelle K K and Mantl S 2013 *IEEE Electron Device Letters* **34** 813–815

[5] Dey A W, Borg B M, Ganjipour B, Ek M, Dick K A, Lind E, Thelander C and Wernersson L E 2013 *IEEE Electron Device Letters* **34** 211–213

[6] Esseni D, Pala M G and Rollo T 2015 *IEEE Transactions on Electron Devices* **62** 3084–3091

[7] Avci U E, Chu-Kung B, Agrawal A, Dewey G, Le V, Rios R, Morris D H, Hasan S, Kotlyar R, Kavalieros J and Young I A 2015 Study of TFET non-ideality effects for determination of geometry and defect density requirements for sub-60mV/dec ge TFET *2015 IEEE International Electron Devices Meeting (IEDM)* (Institute of Electrical and Electronics Engineers (IEEE)) pp 3451–3454

[8] Pala M G and Esseni D 2013 *IEEE Transactions on Electron Devices* **60** 2795–2801

[9] Esseni D and Pala M G 2013 *IEEE Transactions on Electron Devices* **60** 2802–2807

[10] Li M O, Esseni D, Snider G, Jena D and Xing H G 2014 *Journal of Applied Physics* **115** 074508

[11] Szabó Á, Koester S J and Luisier M 2015 *IEEE Electron Device Letters* **36** 514–516

[12] Cao J, Logoteta D, Özkaya S, Biel B, Cresti A, Pala M and Esseni D 2015 A computational study of van der waals tunnel transistors: Fundamental aspects and design challenges *2015 IEEE International Electron Devices Meeting (IEDM)* (Institute of Electrical and Electronics Engineers (IEEE)) pp 12.5.1–12.5.4

[13] Cao J, Logoteta D, Ozkaya S, Biel B, Cresti A, Pala M G and Esseni D 2016 *IEEE Transactions on Electron Devices* **63** 4388–4394

[14] Cao J, Cresti A, Esseni D and Pala M 2016 *Solid-State Electronics* **116** 1–7

[15] Lu S C, Mohamed M and Zhu W 2016 *2D Materials* **3** 011010

[16] Sylvia S S, Alam K and Lake R K 2016 *IEEE Journal on Exploratory Solid-State Computational Devices and Circuits* **2** 28–35 ISSN 2329-9231

[17] Geim A K and Grigorieva I V 2013 *Nature* **499** 419–425

[18] Jena D 2013 *Proceedings of the IEEE* **101** 1585–1602

[19] Özçelik V O, Azadani J G, Yang C, Koester S J and Low T 2016 *Physical Review B* **94**(3) 035125

[20] Roy T, Tosun M, Cao X, Fang H, Lien D H, Zhao P, Chen Y Z, Chueh Y L, Guo J and Javey A 2015 *ACS Nano* **9** 2071–2079
[21] Yan R, Fathipour S, Han Y, Song B, Xiao S, Li M, Ma N, Protasenko V, Muller D A, Jena D and Xing H G 2015 *Nano Letters* **15** 5791–5798
[22] Sarkar D, Xie X, Liu W, Cao W, Kang J, Gong Y, Kraemer S, Ajayan P M and Banerjee K 2015 *Nature* **526** 91–95
[23] Roy T, Tosun M, Hettick M, Ahn G H, Hu C and Javey A 2016 *Applied Physics Letters* **108** 083111
[24] Yan X, Liu C, Li C, Bao W, Ding S, Zhang D W and Zhou P 2017 *Small* **13** 1701478
[25] Liu X, Qu D, Li H M, Moon I, Ahmed F, Kim C, Lee M, Choi Y, Cho J H, Hone J C and Yoo W J 2017 *ACS Nano* **11** 9143–9150
[26] Rozhkov A, Sboychakov A, Rakhmanov A and Nori F 2016 *Physics Reports* **648** 1–104
[27] Britnell L, Gorbachev R V, Jalil R, Belle B D, Schedin F, Mishchenko A, Georgiou T, Katsnelson M I, Eaves L, Morozov S V, Peres N M R, Leist J, Geim A K, Novoselov K S and Ponomarenko L A 2012 *Science* **335** 947–950
[28] Britnell L, Gorbachev R V, Geim A K, Ponomarenko L A, Mishchenko A, Greenaway M T, Fromhold T M, Novoselov K S and Eaves L 2013 *Nature Communications* **4** 1794
[29] Huang S, Ling X, Liang L, Kong J, Terrones H, Meunier V and Dresselhaus M S 2014 *Nano Letters* **14** 5500–5508
[30] van der Zande A M, Kunstmann J, Chernikov A, Chenet D A, You Y, Zhang X, Huang P Y, Berkelbach T C, Wang L, Zhang F, Hybertsen M S, Muller D A, Reichman D R, Heinz T F and Hone J C 2014 *Nano Letters* **14** 3869–3875
[31] Tan Y, Chen F W and Ghosh A W 2016 *Applied Physics Letters* **109** 101601
[32] Zhou K, Wickramaratne D, Ge S, Su S, De A and Lake R K 2017 *Physical Chemistry Chemical Physics* **19** 10406–10412
[33] Nayak P K, Horbatenko Y, Ahn S, Kim G, Lee J U, Ma K Y, Jang A R, Lim H, Kim D, Ryu S, Cheong H, Park N and Shin H S 2017 *ACS Nano* **11** 4041–4050
[34] Lu A K A, Houssa M, Luisier M and Pourtois G 2017 *Physical Review Applied* **8**(3) 034017
[35] Mishchenko A, Tu J S, Cao Y, Gorbachev R V, Wallbank J R, Greenaway M T, Morozov V E, Morozov S V, Zhu M J, Wong S L, Withers F, Woods C R, Kim Y J, Watanabe K, Taniguchi T, Vdovin E E, Makarovsky O, Fromhold T M, Fal'ko V I, Geim A K, Eaves L and Novoselov K S 2014 *Nature Nanotechnology* **9** 808–813
[36] Lane T L M, Wallbank J R and Fal'ko V I 2015 *Applied Physics Letters* **107** 203506
[37] Chari T, Ribeiro-Palau R, Dean C R and Shepard K 2016 *Nano Letters* **16** 4477–4482
[38] Wallbank J R, Ghazaryan D, Misra A, Cao Y, Tu J S, Piot B A, Potemski M, Pezzini S, Wiedmann S, Zeitler U, Lane T L M, Morozov S V, Greenaway M T, Eaves L, Geim A K, Fal'ko V I, Novoselov K S and Mishchenko A 2016 *Science* **353** 575–579
[39] Perebeinos V, Tersoff J and Avouris P 2012 *Physical Review Letters* **109**(23) 236604
[40] Kim Y, Yun H, Nam S G, Son M, Lee D S, Kim D C, Seo S, Choi H C, Lee H J, Lee S W and Kim J S 2013 *Physical Review Letters* **110**(9) 096602
[41] Amorim B, Ribeiro R M and Peres N M R 2016 *Physical Review B* **93**(23) 235403
[42] Vdovin E E, Mishchenko A, Greenaway M T, Zhu M J, Ghazaryan D, Misra A, Cao Y, Morozov S V, Makarovsky O, Fromhold T M, Patanè A, Slotman G J, Katsnelson M I, Geim A K, Novoselov K S and Eaves L 2016 *Physical Review Letters* **116**(18) 186603
[43] Liu K, Zhang L, Cao T, Jin C, Qiu D, Zhou Q, Zettl A, Yang P, Louie S G and Wang F 2014 *Nature Communications* **5** 4966
[44] Huang S, Liang L, Ling X, Puretzky A A, Geohegan D B, Sumpter B G, Kong J, Meunier V and Dresselhaus M S 2016 *Nano Letters* **16** 1435–1444
[45] Bistritzer R and MacDonald A H 2011 *Proceedings of the National Academy of Sciences* **108** 12233–12237
[46] dos Santos J M B L, Peres N M R and Neto A H C 2012 *Physical Review B* **86** 155449

[47] Wang Y, Wang Z, Yao W, Liu G B and Yu H 2017 *Physical Review B* **95**(11) 115429
[48] Kaasbjerg K, Thygesen K S and Jacobsen K W 2012 *Physical Review B* **85** 115317
[49] Polizzi E and Abdallah N B 2002 *Physical Review B* **66** 245301
[50] Shin M 2009 *Journal of Applied Physics* **106** 054505
[51] Fetter A L and Walecka J D 2003 *Quantum theory of many-particle systems* (Dover Publications Inc., United States)